INTERNATIONAL JOURNAL FOR NUMERICAL METHODS IN FLUIDS
Int. J. Numer. Meth. Fluids 2009; **60**:237–261
Published online 16 September 2008 in Wiley InterScience (www.interscience.wiley.com). DOI: 10.1002/fld.1882

Incorporating spatially variable bottom stress and Coriolis force into 2D, *a posteriori*, unstructured mesh generation for shallow water models

D. Michael Parrish[1,‡] and Scott C. Hagen[2,*,†]

[1]*Dewberry, Fairfax, VA 22031-4666, U.S.A.*
[2]*Department of Civil and Environmental Engineering, University of Central Florida, Orlando, FL 32816-2450, U.S.A.*

SUMMARY

An enhanced version of our localized truncation error analysis with complex derivatives (LTEA−CD) *a posteriori* approach to computing target element sizes for tidal, shallow water flow, LTEA+CD, is applied to the Western North Atlantic Tidal model domain. The LTEA+CD method utilizes localized truncation error estimates of the shallow water momentum equations and builds upon LTEA and LTEA−CD-based techniques by including: (1) velocity fields from a nonlinear simulation with complete constituent forcing; (2) spatially variable bottom stress; and (3) Coriolis force. Use of complex derivatives in this case results in a simple truncation error expression, and the ability to compute localized truncation errors using difference equations that employ only seven to eight computational points. The compact difference molecules allow the computation of truncation error estimates and target element sizes throughout the domain, including along the boundary; this fact, along with inclusion of locally variable bottom stress and Coriolis force, constitute significant advancements beyond the capabilities of LTEA. The goal of LTEA+CD is to drive the truncation error to a more uniform, domain-wide value by adjusting element sizes (we apply LTEA+CD by re-meshing the entire domain, not by moving nodes). We find that LTEA+CD can produce a mesh that is comprised of fewer nodes and elements than an initial high-resolution mesh while performing as well as the initial mesh when considering the resynthesized tidal signals (elevations). Copyright © 2008 John Wiley & Sons, Ltd.

Received 24 July 2007; Revised 11 June 2008; Accepted 12 June 2008

KEY WORDS: localized truncation error analysis; unstructured mesh generation; shallow water equations; tidal computations; complex derivatives; Western North Atlantic Tidal model domain

*Correspondence to: Scott C. Hagen, Department of Civil and Environmental Engineering, University of Central Florida, ENGR2 RM 211, 4000 Central Florida Blvd., Orlando, FL 32816-2450, U.S.A.
†E-mail: shagen@ucf.edu
‡Manuscript prepared while at the University of Central Florida, Orlando, FL 32816-2450, U.S.A.

1. INTRODUCTION

The primary focus of this paper is to present an application of our new algorithm for computing target element sizes for finite element meshes of oceanic and coastal tidal models. The research presented herein is an extension of our earlier work [1] in which we developed and demonstrated a new method for automatically estimating localized truncation error and target element sizes for unstructured meshes.

A finite element model of a physical system requires a geometric description of the system in the form of a mesh of interconnected nodes and elements. In general, the level of detail of the mesh affects the accuracy and stability of the model. In this paper, we extend our new method for generating meshing criteria for two-dimensional models of shallow, tidal flow by incorporating spatially variable bottom stress and Coriolis force.

Existing methods of computing target element sizes for coastal areas leave room for improvements. The *a posteriori* localized truncation error analysis (LTEA) [2–5] is more versatile than other methods, such as the wavelength to grid size ratio [6, 7] and the topographic length scale [8–10] because of its (LTEA's) basis in the shallow water (momentum) equations. However, a major disadvantage of LTEA is that in order to compute values of the localized truncation error—upon which are based the target element sizes—a 9×9 finite difference (FD) molecule, centered at mesh nodes, is applied in computing the derivative terms (up to fifth order) of the localized truncation error estimate. Points in the FD molecule must lie in different elements of a linear triangular mesh of the model from which localized truncation error is to be computed. This requirement results in numerous cases where the FD molecule violates the mesh boundaries. These cases include all boundary nodes and all nodes in the vicinity of the boundary. Therefore LTEA is suitable only for applications where the mesh area is large in comparison to its boundary, that is $nn/nb \gg 1$, where *nn* is the number of nodes in the mesh and *nb* is the number of boundary nodes. Boundary shape alone is not the determining factor; rather it is how that shape is discretized.

Therefore we developed an algorithm that all but eliminates the limitations imposed by the FD molecule while maintaining the desirable qualities of LTEA, namely maintaining the basis in localized truncation error of the momentum equations, calculable from the velocity field. We achieve this by recasting the localized truncation error estimate in terms of complex derivatives ($\partial/\partial z$ instead of $\partial/\partial x$ and $\partial/\partial y$, where $z = x + \hat{\imath} y$ and the lateral coordinates of the mesh lie in the x/y plane); hence we name the new method LTEA+CD. We use the plus sign to indicate the inclusion of Coriolis force and locally variable bottom stress in the method, omitted from our earlier LTEA−CD [1]. This allows the production of a truncated Taylor series (the mathematical basis of LTEA), the zero to sixth-order ($\partial^6/\partial z^6$) terms of which are calculable using only seven discrete points in a difference molecule, all of which may be located within the 'valence shell' of elements surrounding a typical interior node in a linear triangular mesh. For cases where the node is on the boundary, eight points may be applied to estimate the zero to seventh-order ($\partial^7/\partial z^7$) terms. The extra point is needed in order to provide $O[(\Delta_M)^2]$ accuracy, where Δ_M is the size of a mesh element (units of length).

After developing the theory of and explaining the procedure for applying LTEA+CD, we apply the method to the production of a new mesh for the Western North Atlantic Tidal (WNAT) model domain.

In order to produce target element sizes, a nonlinear tidal simulation is executed with an initial mesh. For ease of mesh generation, this could be a uniform mesh, but uniformity is not required;

DOI: 10.1002/fld

herein, we use an existing mesh. The LTEA+CD algorithm computes target element sizes from model output; the target element sizes are linearly scaleable. It is up to the user to select the scale factor; we select a value such that the resulting mesh would have adjacent elements that are no more that a factor of two different in area. (We note briefly that the scale factor may also be selected so as to produce a mesh having a certain number of nodes or elements, but we will not discuss this further since this technique is not applied to the application presented herein.) Note that were the flow field sufficiently known from field data, no simulation would be necessary in order to compute the target element sizes. However, at this time, for most cases, flow fields must be computed due the scarcity and unavailability of accurate, measurement-based data.

In a review by Greenberg *et al*. [11], several issues pertaining to mesh resolution and the accuracy of coastal and ocean circulation models are examined. Based upon their review, it seems that there are only about three quantitative relations (though many qualitative ones) that should influence mesh resolution: the Courant number, $(\Delta t)(gh)^{1/2}(\Delta_{\mathrm{M}})^{-1}$, where Δt is the timestep, g is the acceleration due to gravity, and h is bathymetric depth [12–16]; the topographic length scale, $h/\|\nabla h\|$ [8–10]; and localized truncation error [3, 5, 17, 18], which requires the evaluation of twenty derivative terms, up to the fifth order. Note that meshing according to the Courant number or the topographic length scale would not incorporate bottom stress, and that LTEA, while compatible with regionally varying bottom stress, is not applicable at the domain boundary.

Hagen *et al*. [4] developed LTEA first for one-dimensional problems and examined performance on an idealized ocean domain. They experimented with different imposed maximum multiple of change criteria in producing one-dimensional meshes from LTEA results. This concept of maximum multiple of change is included in the present work, with modification. Hagen *et al*. [5] applied the two-dimensional LTEA to a realistic Gulf of Mexico domain and demonstrated that LTEA may be applied to produce a mesh that performs better compared to a mesh having approximately the same number of nodes and elements, produced by targeting a specific Courant number.

The characteristic that distinguishes LTEA−CD from LTEA the most is the ability of LTEA−CD to compute target element sizes at and near the boundary. This capability opens up new possibilities in the field of meshing for coastal circulation problems.

Both LTEA and LTEA−CD are *a posteriori* methods, that is, they rely upon the results of a simulation in order to compute optimal meshing requirements for future simulations. By 'optimal' we mean that the mesh is designed so as to distribute truncation error uniformly. In practice, the distribution of truncation error does not become absolutely uniform, but is made more uniform.

From a theoretical perspective, the chief way in which LTEA−CD differs from LTEA is that the localized truncation error estimate is computed using derivatives with respect to the complex quantity $z=x+\hat{\imath}y$ instead of x and y. The main consequence of this approach is the dramatic simplification of the localized truncation error estimator, which translates into reduced computing time and the introduction of the capability of computing the estimate at and near the boundary.

There are many examples of the application of complex derivatives to two-dimensional engineering problems. Those new to complex derivatives may consult [19–24], which provide introductory material and example applications.

The remainder of this section sketches the development of our enhanced algorithm, LTEA+CD. This is followed by a description of the application of LTEA+CD to the creation of a new mesh for the WNAT model domain, which includes the Gulf of Mexico, the Caribbean Sea, and the portion of the North Atlantic Ocean that lies west of the 60° W meridian (Figure 1; further discussion surrounding Figure 1 is reserved until Section 6.2). In subsequent sections, we present details on

DOI: 10.1002/fld

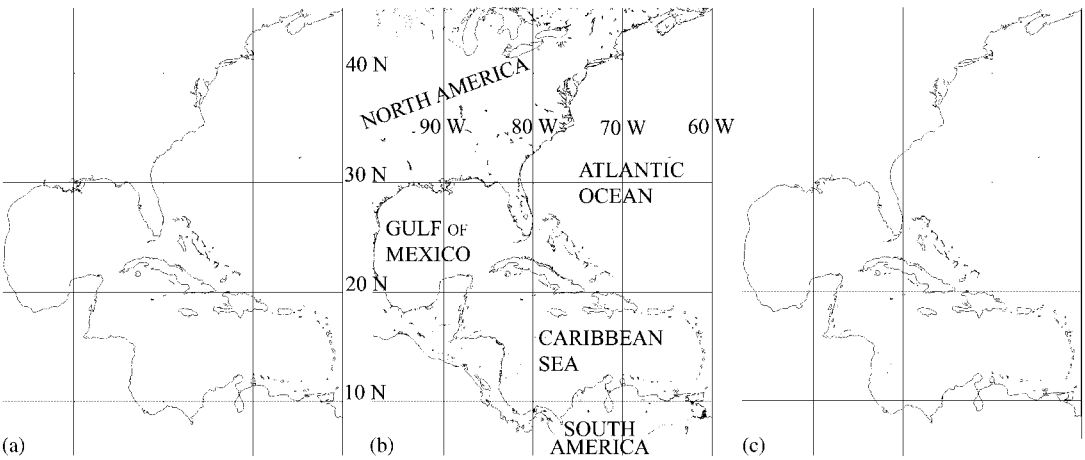

Figure 1. Boundaries used in the study: (a) ec2000v2d; (b) World Data Bank II 1:200 000 coastline for the western North Atlantic Tidal model domain; and (c) NEW. Note the differences between the NEW and ec2000v2d boundaries in the extreme western Caribbean Sea, in the north-central Gulf of Mexico, and Bahamas.

the development of two new meshes for the WNAT model domain by applying LTEA+CD. The presentation of model results is reserved until after we have described each mesh and the processes used for creating them, where we present them in a comparative fashion.

2. THEORY

We consider only localized truncation error of the harmonic, linearized shallow water momentum equations (e.g. [3]). In Cartesian coordinates, the two-dimensional linearized shallow water momentum equations are

$$\frac{\partial u}{\partial t}+g\frac{\partial \eta}{\partial x}+\tau u-fv=0 \quad \text{and} \quad \frac{\partial v}{\partial t}+g\frac{\partial \eta}{\partial x}+\tau v+fu=0$$

where u and v are depth-integrated velocities in the x- and y-directions, t is time, g is the acceleration due to gravity, η is the deviation of the water surface from the geoid, τ is bottom stress, and f is the Coriolis parameter. These temporally dependent equations may be converted to harmonic form by considering a single harmonic constituent of frequency ω, from the tidal signal, and substituting $u=\hat{u}e^{\hat{\imath}\omega t}$, $v=\hat{v}e^{\hat{\imath}\omega t}$, and $\eta=\hat{\eta}e^{\hat{\imath}\omega t}$, yielding

$$(\hat{\imath}\omega+\tau)\hat{u}-f\hat{v}+g\frac{\partial \hat{\eta}}{\partial x}=0 \tag{1a}$$

and

$$(\hat{\imath}\omega+\tau)\hat{v}+f\hat{u}+g\frac{\partial \hat{\eta}}{\partial y}=0 \tag{1b}$$

DOI: 10.1002/fld

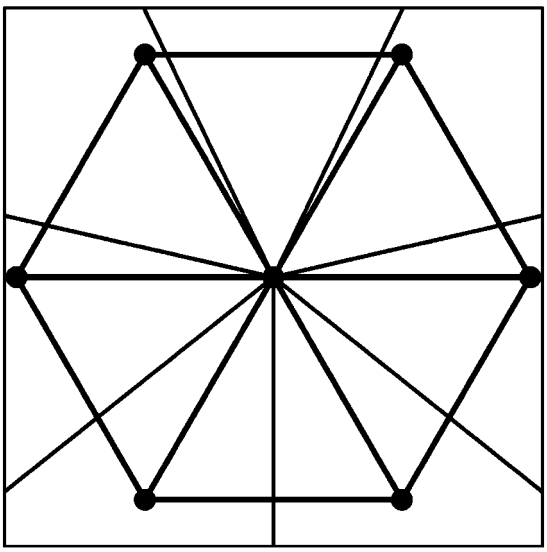

Figure 2. An interior submesh (thick lines and dots) underlies the mesh (medium weight lines; portions of seven elements are shown). The submesh consists of a central node surrounded by a 'valence shell' of equilateral triangular elements. The central node coincides with a node on the interior of the mesh.

where $\hat{\imath}^2 = -1$, $\hat{u}$ and $\hat{v}$ are harmonic velocities in the x- and y-directions, and $\hat{\eta}$ is harmonic deviation of the water surface from the geoid.

The momentum equations, (1a) and (1b), are discretized spatially over a submesh using Galerkin, linear triangular finite elements. We define a submesh to be a central node surrounded by a valence shell of equilateral triangular elements, each consisting of three nodes, one of which is the central node (Figure 2). The submesh does not necessarily coincide with the elements of a mesh on which the solution is computed (note, for example, in Figure 2, we have drawn the submesh underlying a mesh node having a valence of seven, one more than the submesh itself); hence we avoid the term 'stencil'. However, the central node is located on a node of the mesh from which the solution is derived. The discrete form of the momentum equations, (1a) and (1b), are, in the x-direction,

$$\frac{\hat{\imath}\omega+\tau}{12}\left(\sum_{j=1}^{6}\hat{u}_j+6\hat{u}_0\right)+\frac{g}{6\Delta}(2\hat{\eta}_1+\hat{\eta}_2-\hat{\eta}_3-2\hat{\eta}_4-\hat{\eta}_5+\hat{\eta}_6)=0 \tag{2a}$$

and in the y-direction,

$$\frac{\hat{\imath}\omega+\tau}{12}\left(\sum_{j=1}^{6}\hat{v}_j+6\hat{v}_0\right)+\frac{g}{2\sqrt{3}\Delta}(\hat{\eta}_2+\hat{\eta}_3-\hat{\eta}_5-\hat{\eta}_6)=0 \tag{2b}$$

(Equations 6.22 and 6.23 in [2]), where the subscripts are the local indices of the central node (0) and its neighbors (1 to 6, counter clockwise from the $+x$-axis, a different scheme than in Hagen [2]) and Δ is the distance from the central node to that of any of its neighbors within the submesh (Hagen [2] defined the distance between neighboring nodes as 2Δ, convenient when working in x- and y-coordinates). Note that for the moment, we have dropped the Coriolis terms.

DOI: 10.1002/fld

Departing further from Hagen [2], we develop an expression for truncation error that is based upon an analysis in the complex plane. Let $z=x+\hat{\imath}y$. We place the origin of the complex plane at a central node. The discrete momentum equations (2a) and (2b) may be expressed in terms of $f_0 \in \{\hat{\eta}_0, \hat{u}_0, \hat{v}_0\}$ and its derivatives $f_0^{(k)},\ k \in \{0, 1, 2, \ldots\}$, by substituting the complex Taylor series for the $f_j \in \{\hat{\eta}_j, \hat{u}_j, \hat{v}_j\}$, i.e.

$$f_j = f_0 + \frac{\Delta_j}{1!} f_0^{(1)} + \frac{\Delta_j^2}{2!} f_0^{(2)} + \cdots + \frac{\Delta_j^6}{6!} f_0^{(6)} + \text{HOT} \tag{3}$$

where $\operatorname{mod}\Delta_j = \Delta,\ \Delta_j = (x_j - x_0) + \hat{\imath}(y_j - y_0),\ j \in \{1, 2, \ldots, 6\}$, and HOT are the higher order terms. Again, by substituting the complex Taylor series (Equation (3)) into the discrete momentum Equations (2a) and (2b), and applying our chosen configuration of nodes and elements, the Taylor series expansions of the discrete momentum equations become, after cancellation of terms, respectively,

$$\frac{\hat{\imath}\omega+\tau}{1440}(1440\hat{u}_0 + \Delta^6 \hat{u}_0^{(6)}) + \frac{g}{120}(120\hat{\eta}_0^{(1)} + \Delta^4 \hat{\eta}_0^{(5)}) = 0 \tag{4a}$$

and

$$\frac{\hat{\imath}\omega+\tau}{1440}(1440\hat{v}_0 + \Delta^6 \hat{v}_0^{(6)}) + \frac{\hat{\imath}g}{120}(120\eta_0^{(1)} - \Delta^4 \eta_0^{(5)}) = 0 \tag{4b}$$

where we have dropped the HOT. We multiply Equation (4a) by $\hat{\imath}$ and add the result to Equation (4b), which yields

$$(\hat{\imath}\omega+\tau)(\hat{\imath}\hat{u}_0 + \hat{v}_0) + 2\hat{\imath}g\hat{\eta}_0^{(1)} + \Delta^6 \frac{\hat{\imath}\omega+\tau}{1440}(\hat{\imath}\hat{u}_0^{(6)} + \hat{v}_0^{(6)}) = 0 \tag{5}$$

A localized truncation error estimator is determined by subtracting (1b) and $\hat{\imath}\times$ (1a) from (5):

$$\hat{\tau}_{\text{ME}} = \Delta^6 \frac{\hat{\imath}\omega+\tau}{1440}(\hat{\imath}\hat{u}_0^{(6)} + \hat{v}_0^{(6)}) \tag{6}$$

The terms involving $\hat{\eta}$ cancel through application of the chain rule and because $\partial x/\partial z = \frac{1}{2}$ and $\partial y/\partial z = 1/2\hat{\imath}$ (see, e.g. [25]).

We create a new algorithm, LTEA+CD, enhancing LTEA−CD by the inclusion of spatially variable bottom stress and the Coriolis force. Linear Galerkin finite elements are again applied. The corresponding truncation error expression is

$$\hat{\tau}_{\text{ME}}^{+} = \frac{\Delta^6}{1440}[\omega(\hat{\imath}v_0 - \hat{u}_0) + (\tau\hat{v})_0 + \hat{\imath}(\tau\hat{u}_0) - \hat{\imath}(f\hat{v})_0 + (f\hat{u})_0]^{(6)} \tag{7}$$

The development of Equation (7) is the same as that of Equation (6), except that the Coriolis terms are kept and that Equation (7) is linearized by considering the products involving τ and f to vary linearly over an element, rather than taking τ to be constant and assuming $f=0$. Not making this assumption would greatly increase the complexity of computing the derivative term. In addition, inclusion of nonlinear terms would prevent the use of the harmonic form. In this paper, we prefer the computational advantages of these assumptions to more mathematically rigorous approaches that, in a preliminary assessment [1], produce the same end.

DOI: 10.1002/fld

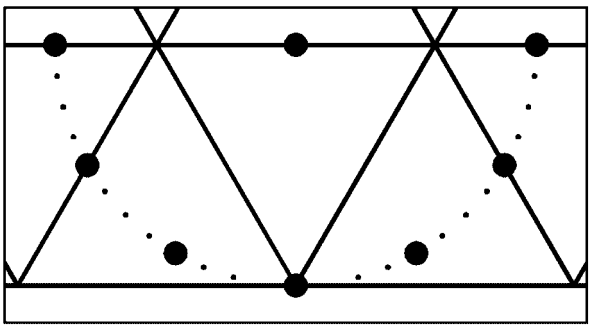

Figure 3. A boundary difference molecule (heavy dots; light dots included to illustrate shape only) underlies the mesh (medium weight lines). The shape and orientation of the submesh allows for concave boundaries. In this example, the central node of the boundary submesh is located bottom center.

For interior nodes, the derivative is calculated by a difference equation where the functional values are interpolated onto a hexagonal difference molecule of seven points, identical to the submesh described above, and the complex field is approximated by a complex polynomial. For boundary nodes, the process is the same, except that the difference molecule is semi-circular in shape, has eight points, and the central node lies on the midpoint of the semicircle (Figure 3). The points of the boundary difference molecule lie along the semicircle at intervals of 30°; an eighth point is placed at the center of the semicircle. It is the compact nature of these difference molecules that enables us to compute the derivative terms in Equation (7) at and near the domain boundary.

The discrete physics upon which the localized truncation error estimates are based are consistent with the assumptions of the Advanced Circulation Model for Oceanic, Coastal, and Estuarine Waters-two dimensional depth integrated option (ADCIRC-2DDI version 42.06, henceforth ADCIRC), applied herein. A brief description of ADCIRC is given in a previous article [26]; for details, see [27, 28].

Target element sizes, Δ_*, are computed by rearranging Equation (7) into the form

$$\Delta_* = aD \tag{8}$$

where a is an arbitrary scale factor and D is a deterministic factor. This is equivalent to selecting a target value for $\hat{\tau}^+_{\mathrm{MR}}$ and solving for Δ. Note that different a's could be chosen for different regions of a model domain; for example, the area of interest may have a lower a than that of the remainder of the domain. Herein, we apply a globally constant a for each mesh created.

3. APPLICATION OVERVIEW

In developing a new mesh for the WNAT model domain that includes variable bottom stress, our first task is to estimate bottom stress. This is accomplished through the utilization of the results of a simulation over an existing finite element mesh, ec2000v2d, that produces generally good results [29]. Next, we apply LTEA+CD to the model results over ec2000v2d (velocity harmonics) and corresponding bottom stresses so as to generate an intermediate mesh, INTR. Finally, we create target element sizes from simulation results over INTR, construct the corresponding final mesh, FIN, and run the model using it. The boundary for INTR is generated afresh and is applied in

DOI: 10.1002/fld

the creation of FIN. Simulation results (tidal elevation amplitudes and phases) are compared to measurement-based tidal constituents from 147 stations. The results over ec2000v2d serve as a benchmark.

Entire meshing is performed with SMS version 9.0 [30]. The INTR and FIN meshes are produced nearly automatically from the target elements sizes established by LTEA+CD. The FIN mesh was produced in a series of patches which were then 'stitched' together manually. Also, several spurious elements appeared adjacent to the mainland boundary (in violation of the target element sizes); these were eliminated by a manual, but largely systematic process. Finally, a few skinny elements were eliminated manually. Manual editing required approximately 8 h for a proficient SMS user (Parrish). Other than these noted exceptions, mesh construction was automatic.

4. MODEL PARAMETERS

All parameters are identical for all simulations, except for the meshes themselves, and for the open boundary forcing, which, for INTR and FIN, is interpolated linearly from the boundary forcing of the ec2000v2d simulation. The open boundary is forced with seven tidal elevation constituents (Q_1, O_1, K_1, N_2, M_2, S_2, and K_2). Tidal potential terms are included throughout the domain for the same frequencies. A harmonic analysis is performed on the time series results with 23 tidal constituents (Table I) at increments of 5 min (300 s), over the last 45 days of simulated time.

Bottom stress is computed according to the hybrid quadratic friction formulation

$$\tau = C_{f\,\min}\left[1+\left(\frac{H_{\text{break}}}{H}\right)^{\theta}\right]^{\gamma/\theta}\frac{\sqrt{u^2+v^2}}{H} \tag{9}$$

in which τ is the bottom stress, $C_{f\,\min} = 0.0025$, $H_{\text{break}} = 10.0\,\text{m}$, H is the total water column depth, $\theta = 10, \gamma = \frac{1}{3}$, and u and v are the depth-integrated velocities (x- and y-directions). A spatially constant horizontal eddy viscosity of $5.0\,\text{m}^2/\text{s}$ is applied. Advective terms are not included—note that throughout most of the WNAT model domain, shallow water flow is weakly nonlinear. Wetting and drying is employed with a minimum depth of 0.1 m.

Each simulation is run for a simulated duration of 90 days using a time step of 4.0 s. A 20-day hyperbolic ramp function is applied to the open boundary forcing. Variable Coriolis force is applied. The bathymetry from ec2000v2d is taken as the digital elevation model (DEM) for the INTR and FIN meshes.

5. INITIAL SIMULATION

An initial simulation is executed over an existing mesh, ec2000v2d [29], the boundary of which is presented in Figure 1(a) (the mesh itself is too dense to be presented here). The resolution of ec2000v2d is based upon the wavelength to grid size ratio and topographic length scale [8–10]; it was developed for the generation of a tidal constituent data base for the WNAT model domain. Mukai *et al*. [29] selected a target wavelength to gridsize ratio of '100 or more' and a TLS of 1.0. In addition, elements larger than 25 km were not allowed. Because their mesh was largely constructed using manual techniques, there were large deviations from the target criteria, usually toward the conservative side (i.e. nodes were more dense than the target would indicate). Thus far,

DOI: 10.1002/fld

all of the meshes of the WNAT model domain that our research program has produced are derived from ec2000v2d.

6. INTERMEDIATE SIMULATION

An intermediate mesh is based upon the application of LTEA+CD with the model output of the initial simulation.

6.1. Estimation of bottom stress

The harmonic output (23 tidal constituents, Table I) from the initial simulation is used to resynthesize time series of currents and water surface elevations. These time series are used in order to estimate bottom stress for application in LTEA+CD (Equation (9)). A spatially variable, temporally averaged bottom stress is estimated by computing, for each node of the mesh, the mean value of τ, calculated at discrete time steps over the first spring–neap cycle in a tidal epoch. We use

Table I. Tidal constituents (names, frequencies, and periods) included in harmonic analysis of ADCIRC model results.

	Tidal constituent	Frequency (rad/s)	Period (h)	Nodes	Node fraction (%)	Area fraction (%)
	NOT_CALCULATED			25962	10.20	5.70
	STEADY	0.000 000 000 000 000		15244	5.99	6.04
	MN	0.000 002 639 203 022	27.55 da	825	0.32	0.50
	SM	0.000 004 925 201 824	14.77 da	3828	1.50	1.40
*	Q_1	0.000 064 958 541 130	26.87	81	0.03	0.31
*	O_1	0.000 067 597 744 150	25.82	8346	3.28	2.53
	P_1	0.000 072 522 946 000	24.07	198	0.08	0.73
*	K_1	0.000 072 921 158 360	23.93	23239	9.13	7.03
	MNS_2	0.000 132 954 497 700	13.13	0	0.00	0.00
	$2MS_2$	0.000 135 593 700 700	12.87	198	0.08	0.00
*	N_2	0.000 137 879 699 500	12.66	899	0.35	0.66
*	M_2	0.000 140 518 902 500	12.42	154366	60.64	67.93
	$2MN_2$	0.000 143 158 105 500	12.19	1	0.00	0.00
*	S_2	0.000 145 444 104 300	12.00	9628	3.78	5.91
*	K_2	0.000 145 842 317 200	11.97	384	0.15	0.37
	$2SM_2$	0.000 150 369 306 200	11.61	23	0.01	0.00
	MN_4	0.000 278 398 602 000	6.27	12	0.00	0.00
	M_4	0.000 281 037 805 000	6.21	3657	1.44	0.27
	MS_4	0.000 285 963 006 800	6.10	442	0.17	0.01
	$2MN_6$	0.000 418 917 504 500	4.17	382	0.15	0.04
	M_6	0.000 421 556 707 500	4.14	5745	2.26	0.49
	MSN_6	0.000 423 842 706 300	4.12	156	0.06	0.01
	M_8	0.000 562 075 610 000	3.11	716	0.28	0.05

Harmonic results for those constituents marked with an asterisk (*) are applied in the model forcing. The right three columns show (1) the number of nodes (of ec2000v2d), (2) the node fractions, and (3) the area fractions of the mesh for which a given tidal constituent determines the target element size.

DOI: 10.1002/fld

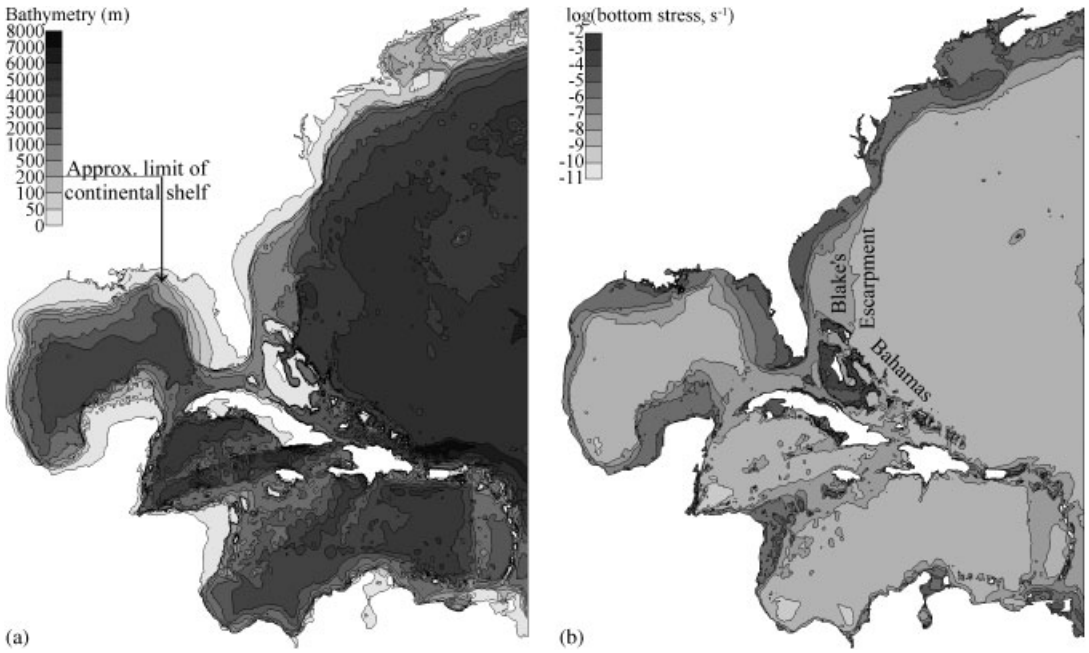

Figure 4. (a) Bathymetry of the ec2000v2d mesh. This data set is also used as the digital elevation model (DEM) for the other meshes. In the lower range, the scale is quasi-logarithm. (b) Logarithm of average bottom stress, s^{-1}, computed from the ec2000v2d run. The variation in bottom stress generally demarcates bathymetric features.

a time step equal to one-twentieth of an M_2 cycle, equivalent to half an M_{10} cycle; M_{10} is the 'fastest' tidal constituent in the harmonic analysis (Table I). A minimum value of $\tau = 10^{-11}\,\mathrm{s}^{-1}$ is imposed where a lower value is computed. This value of $10^{-11}\,\mathrm{s}^{-1}$ is arrived at by computing τ everywhere and examining the minimum non-zero average τ over the entire mesh; $10^{-11}\,\mathrm{s}^{-1}$ is the next lowest power of 10. At each time step, τ is computed by the hybrid quadratic formulation (Equation (9)).

The estimated values of bottom stress are reflective of bathymetric features of the mesh. This can be ascertained by an examination of Figures 4(a) and (b), where Figure 4(a) shows bathymetric contours in increments of 1000 m down to the 1000 m contour (and in quasi-logarithmic increments in shallower regions) and Figure 4(b) shows contours of bottom stress in logarithmic increments. Note, for example, the demarcation of Blake's Escarpment, the continental shelf (approximately the region shoreward of the 200 m contour), and the Bahamas in both Figures 4(a) and (b).

In the deep, most of the bottom stress values are around $10^{-8}\,\mathrm{s}^{-1}$, increasing to (relatively) high values in very shallow water; the highest values are on the order of $0.01\,\mathrm{s}^{-1}$, consistent with the typical range of depths and current speeds. For comparison, we present computed bottom stress values, τ, in Table II. This table shows values of τ as a function of water depth, H, and current speed—in the table, the log of current speed in m/s is given (e.g. $\log 1\,\mathrm{m/s} = 0$. $\log 0.1\,\mathrm{m/s} = -1$). Table II also shows the value of C_f computed from the hybrid quadratic friction formulation, equal to $C_{f\min}$ times the term raised to the γ/θ power in Equation (9), as well as the ratio

DOI: 10.1002/fld

Table II. Variation of bottom stress (τ) with total depth and current speed, according to the hybrid quadratic bottom friction formulation.

	log (current speed, m/s)		$\log(\tau, S^{-1})$				
H (m)	$C_f/C_{f\min}$	C_f	−4	−3	−2	−1	0
1	2.15	0.0054	−6.3	−5.3	−4.3	−3.3	−2.3
2	1.71	0.0043	−6.7	−5.7	−4.7	−3.7	−2.7
5	1.26	0.0031	−7.2	−6.2	−5.2	−4.2	−3.2
10	1.02	0.0026	−7.6	−6.6	−5.6	−4.6	−3.6
20	1.00	0.0025	−7.9	−6.9	−5.9	−4.9	−3.9
50	1.00	0.0025	−8.3	−7.3	−6.3	−5.3	−4.3
100	1.00	0.0025	−8.6	−7.6	−6.6	−5.6	−4.6
200	1.00	0.0025	−8.9	−7.9	−6.9	−5.9	−4.9
500	1.00	0.0025	−9.3	−8.3	−7.3	−6.3	−5.3
1000	1.00	0.0025	−9.6	−8.6	−7.6	−6.6	−5.6
2000	1.00	0.0025	−9.9	−8.9	−7.9	−6.9	−5.9
5000	1.00	0.0025	−10.3	−9.3	−8.3	−7.3	−6.3
10 000	1.00	0.0025	−10.6	−9.6	−8.6	−7.6	−6.6

Presented are logarithms of bottom stress versus water depth, H, and logarithm of current speed. Note: $C_{f\min}=0.0025$, $H_{\text{break}}=10.0\,\text{m}$, $\theta=10$, and $\gamma=1/3$.

$C_f/C_{f\min}$. Note that our selection of 10.0 m for H_{break} causes $C_f/C_{f\min}$ to increase toward shallower depths beginning at about 10.0 m of depth. The minimum bottom stress shown in Table II is $10^{-10.6}\approx 3\times 10^{-11}\,\text{s}^{-1}$ (for a depth of 10 000 m and a speed of 10^{-4} m/s) while the maximum value shown is $10^{-2.3}\approx 5\times 10^{-3}\,\text{s}^{-1}$ (for a depth of 1 m and a speed of 1 m/s).

Alternatively, the linearized momentum equations could be solved for τ, but this introduces two ambiguities, namely how to handle the case when velocity, appearing in the denominator, is zero, and how to reconcile the two equations for momentum and two values for τ into a single value.

6.2. *New boundary definition*

A new mesh boundary (Figure 1(c)) is defined by manually editing the boundary points of the World Data Bank II coastline definition [31] (Figure 1(b)), with reference to the ec2000v2d boundary. Although there is some ambiguity in the manual process, the following principles were applied. Manageable sections of the boundary were created; vertices of each section were redistributed at a target spacing of 1000 m (a typical segment of coastline from the World Data Bank II data set is about 500 m length). The number of sharp angles is minimized; where possible, changes in bearing are limited to 15° or less. Embayments less than about 7 km across are eliminated. Small protrusions (long dimension less than about 7 km) are eliminated or smoothed over. The 7 km criterion is based on the diameter of a circle circumscribing a regular 24-gon (interior angles are 345° = 360°–15°) having side length 1000 m. Ripples, consisting of alternating protrusions and embayments, are eliminated. Elimination is generally achieved by filling in the shallow (in the lateral direction), though perhaps wide (wider than 7 km) embayments, although where this would cause a large-scale distortion in the geometry, the adjacent protrusions are eliminated or smoothed over instead. It is also noted that the new boundary was constructed *without* regard for the location of tidal stations.

DOI: 10.1002/fld

The result is a boundary that is smoother than that of ec2000v2d has slightly more detail (except for the Louisiana coast, which is the area of interest for ec2000v2d), including some additional islands, although some islands that appear in ec2000v2d do not appear in the new boundary, consistent with the principles discussed (cf. Figures 1(a) and (c)).

It is apparent that an automatic process for boundary simplification is needed; however, we are aware of none suited to our desire to control for curvature. In addition, such a process would have numerous free parameters, as evidenced by our criteria. The manual editing required the primary author about 40 h to complete; this corresponds to a rate of over 900 km of coastline per hour! Note that boundary definition is really separate from LTEA+CD, and that we could have used an existing boundary. We opted not to use the ec2000v2d boundary because of the presence of sharp corners and bumpiness that may place constraints upon the meshing algorithm so as to violate the target elements sizes.

Note that this NEW mesh boundary determines the shape of the boundary only, not the distribution of nodes along the boundary. The distribution of nodes throughout the domain, including the boundary, is determined by LTEA+CD.

6.3. Intermediate mesh

Normalized target element sizes for INTR are computed by assuming $a=1$ (Equation (4)). Note that the tidal constituents are considered separately as in [1, 18], and that 23 constituents are used to compute 23 data sets of Δ_*. However, In order to capture nonlinearities that were not part of the work of [1, 18], a single nonlinear simulation with seven tidal constituent forcings produces a tidal signal that is analyzed for 23 tidal constituents. Therefore, each of the tidal constituents has had the opportunity to interact with the others. For this reason, the simulations conducted here and the resulting target element sizes are expected to be more reflective of the physics. A final set of normalized target element sizes is determined by selecting, for each location, $\min(\Delta_*)$ from among the 23 data sets, and smoothing the data with a Gaussian smoothing algorithm, the effect of which is shown in Figure 5. The scale factor a is chosen such that the maximum ratio of adjacent element areas [1] in the resultant mesh is 2 (big:small). Based upon visual inspection, the resultant mesh matches the new boundary well. There are 218 001 nodes and 420 531 elements in INTR (Table III), 14% fewer than in ec2000v2d. In some places, INTR is resolved just enough to represent the domain geometry.

In our Gaussian smoothing algorithm, a weight function, the Gaussian distribution, $A\exp(-x/2\sigma^2)$, is applied to D. The parameters of the Gaussian weight function are set so that one standard deviation, σ, coincides with the mean element size (length) about a given node. Note that x is the distance from the node at which the smoothed value is to be computed and A is set such that the sum of all weights is unity. Values from nodes further than three elements away from a central

Table III. Properties of meshes.

				Element sizes (m)	
Mesh	Nodes	Elements	Time step (s)	Small	Large
ec2000v2d	492 182	254 565	4	191	26 519
INTR	420 531	218 001	4	183	69 496
FIN	867 529	444 910	4	644	78 506

DOI: 10.1002/fld

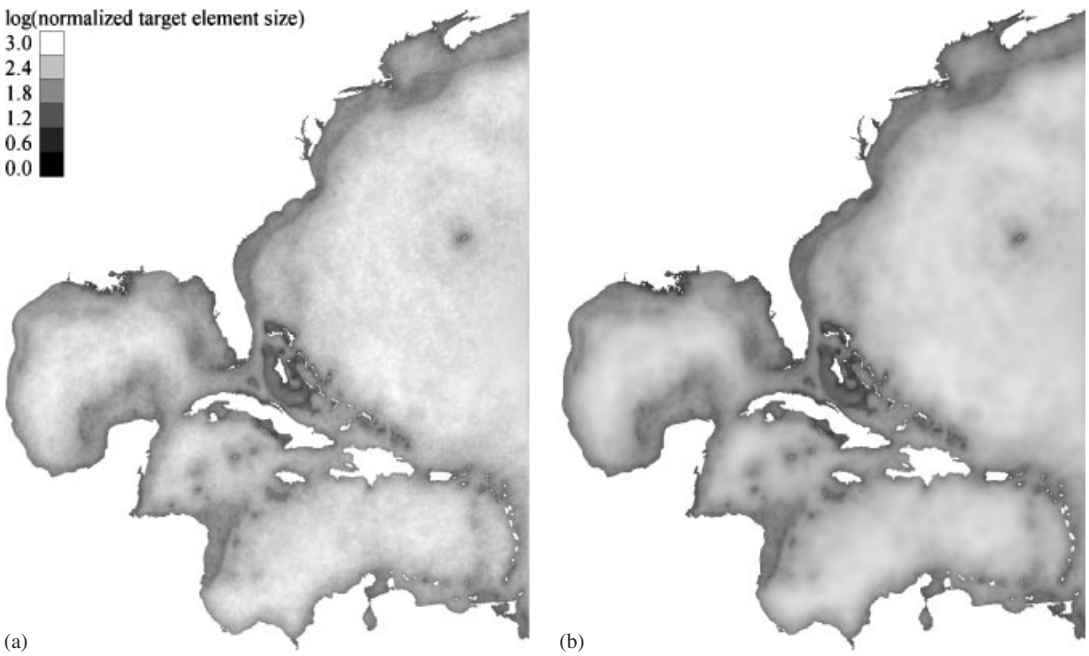

Figure 5. Target element sizes (log of normalized value) derived from the ec2000v2d run: (a) raw values and (b) smoothed values.

node are not used to compute a smoothed value of D. Again, Figure 5 shows the effect of the smoothing algorithm. Figure 5(a) displays the logarithm of the normalized target element size, computed by dividing all values of D by the smallest value of D. Note the noise evident in the normalized data. Figure 5(b) displays the smoothed values computed by applying our smoothing algorithm to the data of Figure 5(a). Note also that our selected value of σ^2 results in smoothed data that still represent the main features of the unsmoothed data.

The application of more advanced smoothing techniques would be expected to produce better results than simple Gaussian smoothing, particularly because Gaussian smoothing ignores significant local, directional variation in localized truncation error that are the result of, for example, the presence of a shipping channel (one would want the smoothing algorithm to smooth only along the channel, not across it). Note that the Gaussian smoothing applied herein is distinct from that applied by Hagen *et al*. [26], whose smoothing algorithm treated the target element sizes as maximum acceptable values, and limited the gradient of the smoothed element sizes, working outward from local minima.

The relative influence of the terms involving ω, f, and τ in the RHS of Equation (7), which determines the distribution of target element size, is location dependent. The ω and f terms are significant throughout the domain, whereas the τ terms, representing the influence of bottom stress, are significant only in the shallower areas. Here, significance indicates that the ratio of the magnitude of the terms in question to the total magnitude of all the terms on the RHS of Equation (7) is at least 10%. Figure 6 depicts graphically the influence (i.e. the ratio mentioned in the previous sentence) of the three groups of terms. Note that the influence of a group of terms

DOI: 10.1002/fld

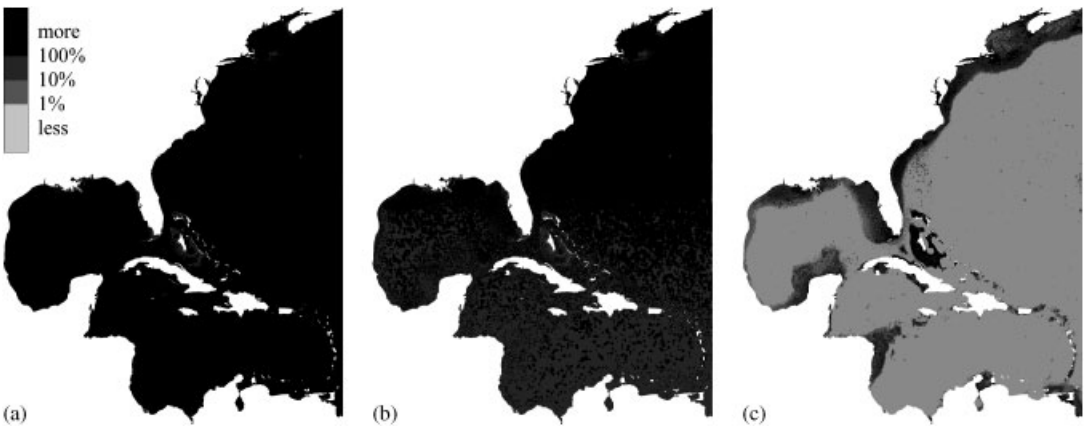

Figure 6. Influence of terms involving (a) ω, (b) f, and (c) τ, for the M_2 tidal constituent. Influence is computed as the ratio of the magnitude of the applicable terms to the magnitude of the total RHS of Equation (7). Terms involving ω and f are relatively important throughout the domain, while terms involving τ are relatively important only in the shallower areas where bottom stress is greater. Influence can be greater than one (100%) because the terms on the RHS of Equation (7) may cancel each other.

can exceed 100%, since terms may cancel one another. Note also that the influence of the Coriolis force (f terms) being on the same order as to that of the ω terms is consistent with the fact that ω ($2\pi/12.42$ h) and f ($2\pi/12.00$ h times the sine of latitude, where the minimum latitude is about 8° N in the WNAT model domain) are similar in magnitude.

The dominance of various tidal constituents in determining the target element size is given in Table I and in Figure 7. In the table, given a tidal constituent, the number of nodes of ec2000v2d for which that tidal constituent dominates is listed, along with the fraction of nodes as a percentage. Table I also lists the area over which a given tidal constituent dominates the determination of target element size, where the area associated with a node is approximated as being proportional to the square of the mean length of element sides that converge at that node.

In Figure 7, we show the nodes for which a particular tidal constituent dominates the determination of target element size. Together, they represent about 87% of the area of the WNAT model domain. M_2 is the dominant tidal constituent in the determination of target element size. However, there are certain broad regions over which other tidal constituents dominate. For example, K_1 tends to dominate a region west of Cuba and northeast of the Yucatan Peninsula. Figure 7 illustrates the importance of considering multiple tidal constituents in applications of LTEA+CD.

Figure 8 shows details of INTR (left) and, for comparison, ec2000v2d (right). Note that there are only three elements between Ft. Desoto (the island at left) and the mainland, and that the resolution provided by INTR seems to be just enough to warrant the inclusion of Ft. Desoto as a no flow boundary (as opposed to meshing over it or connecting it to the mainland). The minimal representation of this area by INTR reflects the effects of the parameter a. The selection of a particular a is, again, arbitrary, but the value selected approaches a 'minimally' acceptable value. A greater value would produce a coarser mesh, in which these detailed features would potentially be obliterated.

DOI: 10.1002/fld

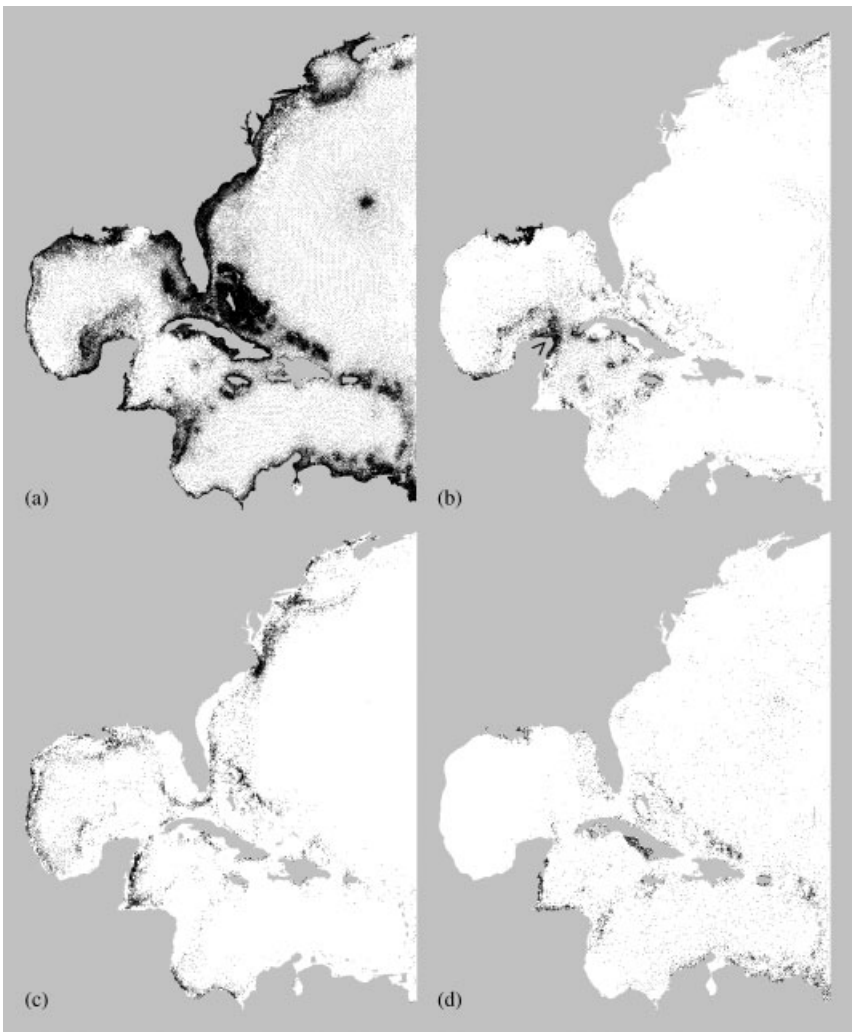

Figure 7. Nodes for which a particular tidal constituent: (a) M_2; (b) K_1; (c) *STEADY*; or (d) S_2 dominates the determination of target element size.

7. FINAL MESH

Target element sizes for FIN are derived from a simulation over INTR, by applying LTEA+CD (Equation (4)) with bottom stress estimated from the simulation results over INTR (contours of bottom stress for either simulation overlie each other). In addition, a minimum element size of 1000 m was specified in order to prevent the number of nodes and elements from being too much greater than ec2000v2d (the unconstrained target element sizes produce a mesh of about 700 000 nodes and 1 400 000 elements). There are 444 910 nodes and 867 529 elements in FIN, about 75% more than ec2000v2d.

DOI: 10.1002/fld

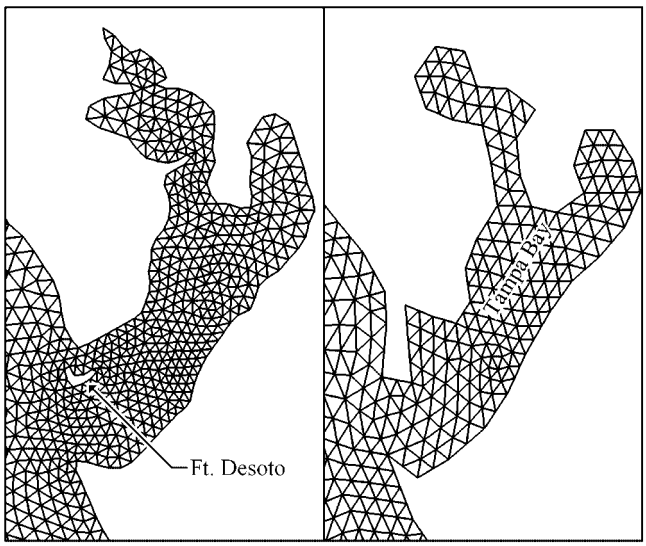

Figure 8. The INTR mesh (left) is, in some locations, just adequate to represent domain geometry. Ft. Desoto (the island) is separated from the mainland by three elements. The INTR mesh contains slightly more detail in comparison to ec2000v2d (right).

We may also compare the meshes themselves (Figures 9 and 10). In general, ec2000v2d contains the highest resolution in the deeper parts of the domain while FIN contains the highest resolution in the shallower waters. The coarsest mesh tends to be INTR, except in very deep water, where FIN is coarser, and in select coastal regions, where ec2000v2d is coarser.

Figure 9 represents the resolution of (a) ec2000v2d, (b) INTR, and (c) FIN in terms of element size (average side length) with a quasi-logarithmic scale. The coarsening of the deep ocean is evident in comparing INTR and FIN to ec2000v2d, while the resolving of the continental shelf break becomes more pronounced (note shelf break along the North American Atlantic coast).

In Figure 10 we present the resolution of the three meshes relative to one another. Figure 10(a) shows which of the three meshes has the highest resolution (the minimum element size) for a given location. The map is based upon grid sizes computed as the average length of element sides coinciding with a common node. These values are then averaged over a regular grid (the pixels of a screen image). Likewise, Figure 10(b) shows which of the three meshes has the lowest resolution (the maximum element size). The ec2000v2d mesh possesses the highest resolution in the deeper waters. Along the Atlantic coast, the continental shelf break is generally most well resolved by FIN. In the deeper regions of the mesh, FIN is the coarsest of the three meshes; ec2000v2d is coarsest in some areas of the Bahamas and between many islands of the Antilles.

8. TIDAL STATIONS

We use for comparison the tidal database assembled by Kojima [32], consisting of tidal elevations and phases of tidal constituents and 203 stations. Of those 203, Kojima [32] found that 150 were suitable for making solution comparisons among runs with several different meshes. He eliminated

DOI: 10.1002/fld

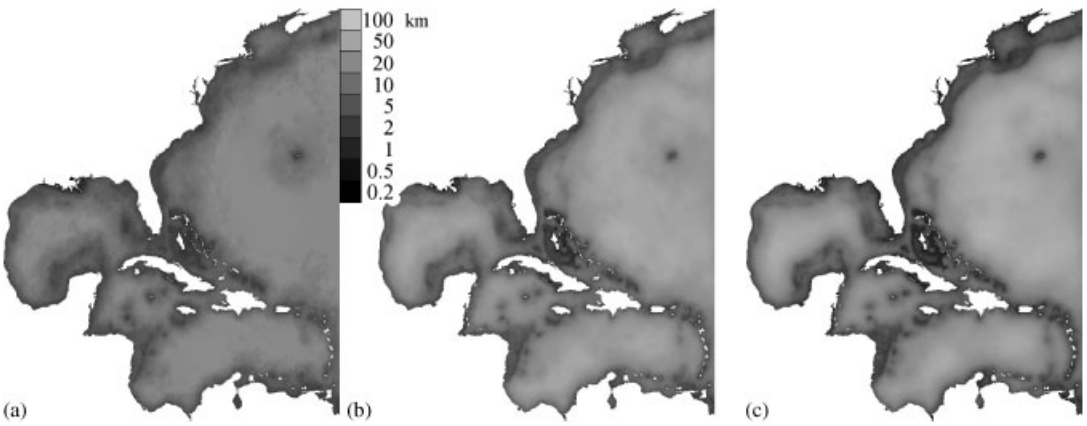

Figure 9. Element sizes (km) for: (a) ec2000v2d; (b) INTR; and (c) FIN meshes.
Note the quasi-logarithmic scale.

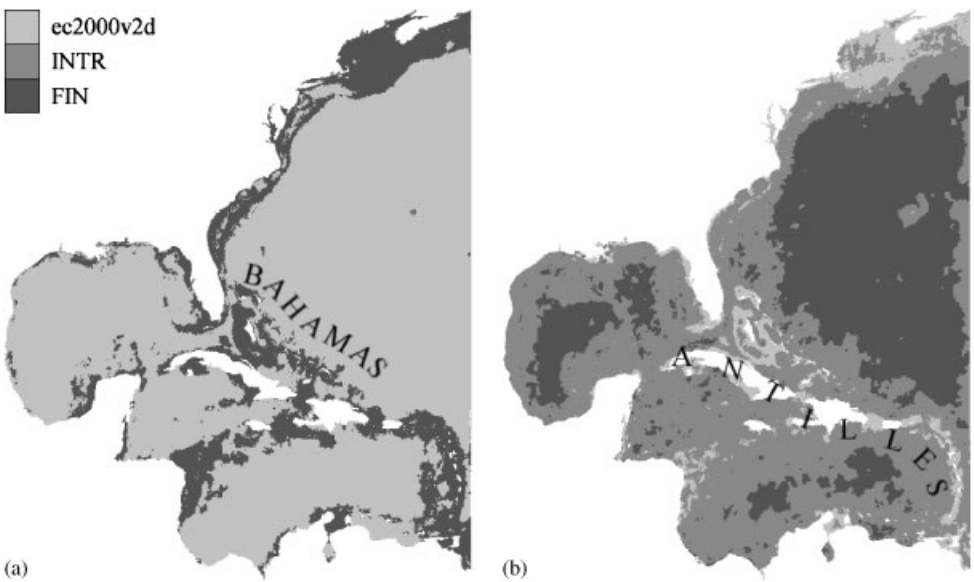

Figure 10. These maps indicate, for a given location, which of the three meshes possesses: (a) the highest resolution (minimum element size) and (b) the lowest resolution (maximum element size).

stations from among the 203 that were (a) located within a bay, inlet, or canal that is not described by one or more of the three meshes, (b) located in an element that went dry (at any time, for any duration) during the period over which harmonic analysis was performed, or (c) influenced by freshwater flow. In the present study, three additional stations went dry during the period of harmonic analysis. Therefore we are left with 147 stations at which comparisons may be made;

DOI: 10.1002/fld

summary statistics are prepared for these stations, but not for individual stations, since we are interested in overall performance, not performance at particular stations. Additionally, consistent with a discussion by Werner [33], we have confirmed that the mean square error over variance (MSE/VAR, details below) statistic applied here is sensitive to the duration and starting point such that for a particular station, the outperformance of one model by another is dependent upon these parameters. Grouping stations reduces the likelihood that one model will outperform another for our period of analysis, but not over all time.

9. MODEL COMPARISON

Resynthesized tidal signals form the bases of our comparisons. Historical signals are resynthesized from all available tidal constituents, and modeled signals are resynthesized from all 23 model output tidal constituents. We note that the sets of historical and model tidal constituent frequencies are different; however, when resynthesized, both are representations of the actual tidal signal.

Three error measures are given. For each, only the first spring-neap cycle of a tidal epoch is considered, and a one-minute time step is applied. The first error measure is the mean square error divided by the population variance of the historical data:

$$\frac{\mathrm{MSE}}{\mathrm{VAR}} = \frac{\mathrm{SSE}}{N \times \mathrm{VAR}} = \frac{\sum_t (\mathrm{Hist}_t - \mathrm{Mod}_t)^2}{\sum_t (\mathrm{Hist}_t - \overline{\mathrm{Hist}})^2} \tag{10}$$

where N is the number of points of comparison. The second and third error measures are computed by shifting the model resynthesized tidal signal in time by increments of one time step (one-minute) and selecting the shift that produces the minimum SSE and therefore the minimum MSE/VAR. The second error measure is therefore MSE/VAR as computed after the shift, while the third error measure is the amount of the shift (absolute value, units of time). Hagen *et al.* [26] applied a similar method in order to distinguish error related to phasing and error related to the wave heights. The approach taken here to compute phase shift lends itself to automatic computation, which we have employed.

The MSE/VAR statistic is equivalent to the square of relative amplitude error for a sinusoidal tidal signal having zero phase error, ε_φ, where relative amplitude error is $\varepsilon_A = |A_{\mathrm{Hist}} - A_{\mathrm{Mod}}|/A_{\mathrm{Hist}}$. For errors in phase only, for phase errors up to about $90°(\pi/2)$, $\mathrm{MSE/VAR} \approx \varepsilon_\varphi/60° = (3/\pi)\varepsilon_\varphi$. More generally, $\mathrm{MSE/VAR} \approx \varepsilon_A^2 + \varepsilon_\varphi^2$, for $\varepsilon_A \lesssim 0.5$ and $\varepsilon_\varphi \lesssim 30° = \pi/6$.

10. RESULTS

We evaluate the performance of the models using the MSE/VAR statistic, averaged over the stations corresponding to each of three groupings, shown in Figure 11. Each group of stations contains at least three stations. Each group of stations is given a unique alphanumeric label; these labels are associated with a group name, also shown in Figure 11 along with the number of stations (in parentheses) comprising the group. The stations are grouped according to major geographical features (i.e. coastline shape, bathymetry) and, to a lesser extent, out of consideration for the geographic dependence of the tides (e.g. along the Atlantic coast of North America, the tides are semi-diurnal, and transition to mixed tide, then to diurnal tides as one moves clockwise around

DOI: 10.1002/fld

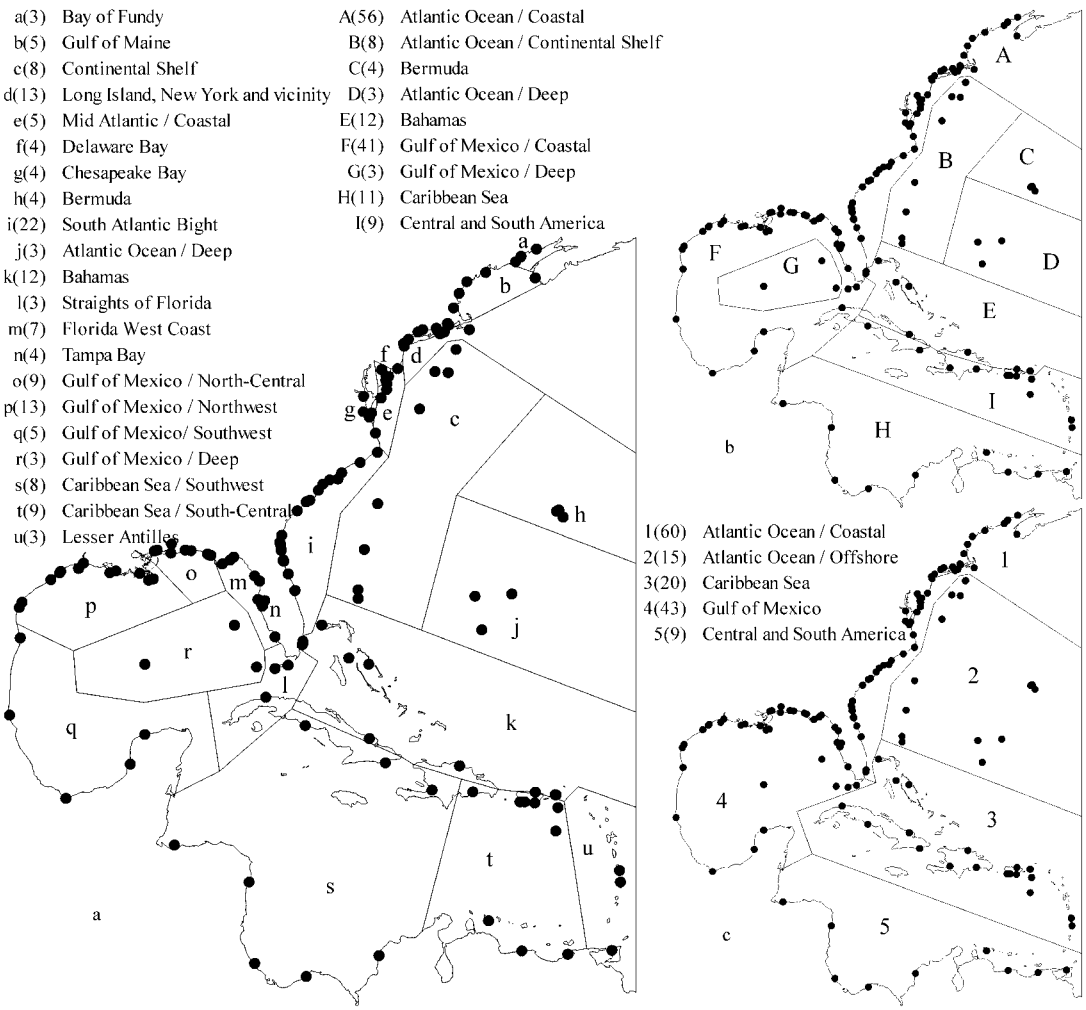

Figure 11. Station groupings; each individual station is represented by a solid dot (•). Statistics (MSE/VAR and phase shift) are averaged over stations in the groups shown. There are three different groupings, each for a different level of consolidation. Numbers in parenthesis indicate the number of stations in each group

the Florida peninsula and onto the Florida panhandle). The line segments demarcating the station groups are meant only to indicate which stations belong to which group, and do not themselves have meaning beyond this.

Examination of MSE/VAR for three different groupings of stations—in Figure 12 and in Table IV—indicates that there is no overall difference among the three models. Note how the symbols for the three plotting areas typically overlap one another. In fact, the means of MSE/VAR values for all of the stations considered differ among the three simulations only in the fourth decimal place, (full tabulation of data is omitted here for the sake of brevity); for comparison,

DOI: 10.1002/fld

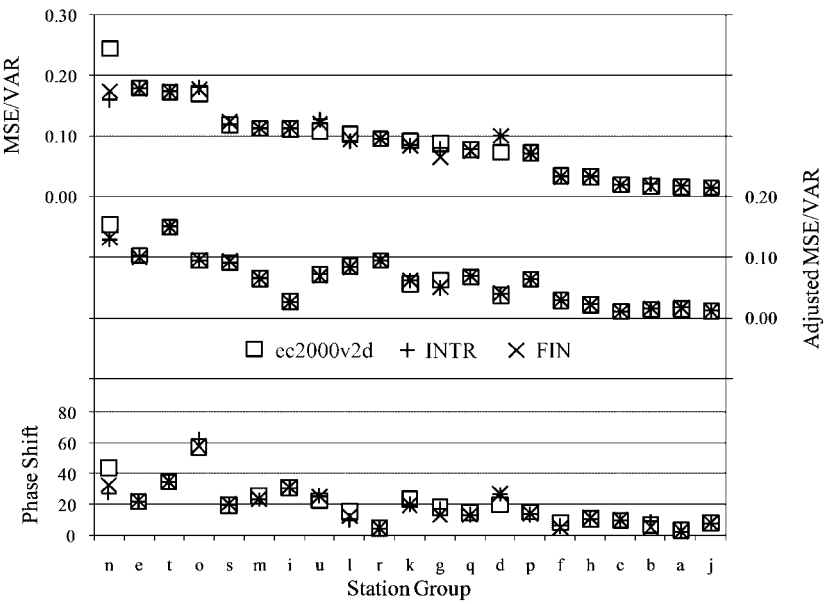

Figure 12. Summary statistics of MSE/VAR (top), adjusted MSE/VAR (middle), and phase shift (bottom) for station groups a–u. There seem to be no overall differences in performance among the three meshes. For particular station groups, there are some notable differences: Tampa Bay and Chesapeake Bay (station groups n and g). The station groups are arranged in descending order (roughly) of MSE/VAR.

Table IV. Summary statistics for ec2000v2d (EC), INTR, and FIN runs.

	MSE/VAR			Adjusted MSE/VAR			Phase shift		
Station group	EC	INTR	FIN	EC	INTR	FIN	EC	INTR	FIN
1	0.0883	0.0916	0.0906	0.0370	0.0366	0.0371	21	22	21
2	0.0225	0.0225	0.0225	0.0136	0.0136	0.0136	10	10	10
3	0.1352	0.1398	0.1388	0.1103	0.1138	0.1133	27	28	27
4	0.1208	0.1137	0.1148	0.0838	0.0812	0.0822	28	26	26
5	0.0970	0.1024	0.1055	0.0681	0.0669	0.0690	21	22	23
A	0.0879	0.0943	0.0932	0.0367	0.0362	0.0365	21	23	22
B	0.0201	0.0202	0.0200	0.0106	0.0106	0.0106	10	10	10
C	0.0332	0.0333	0.0334	0.0216	0.0215	0.0215	11	11	11
D	0.0144	0.0145	0.0146	0.0110	0.0111	0.0111	8	8	8
E	0.0920	0.0843	0.0840	0.0559	0.0610	0.0619	23	20	19
F	0.1203	0.1128	0.1139	0.0816	0.0788	0.0798	29	27	27
G	0.0952	0.0954	0.0955	0.0943	0.0945	0.0946	4	5	4
H	0.1774	0.1798	0.1786	0.1526	0.1542	0.1532	31	32	32
I	0.0970	0.1024	0.1055	0.0681	0.0669	0.0690	21	22	23
Mean	0.0980	0.0983	0.0982	0.0602	0.0597	0.0602	23	23	22

Mean values are computed by giving all stations equal weight.

DOI: 10.1002/fld

the MSE/VAR values are precise to only three significant figures, based upon the precision of the historical data (± 0.0005 m and $\pm 0.005^\circ$ for each tidal constituent).

Plots of adjusted values of MSE/VAR show even less variation among station groups. Only Tampa Bay (station group n) and Chesapeake Bay (station group g) show any appreciable difference among the three simulations.

Tampa Bay exhibits less error for both INTR and FIN, in comparison to ec2000v2d. This is likely due to the increased resolution there; also the boundary definition is smoother and contains an island not present in ec2000v2d (Figure 8). We emphasize that the increased resolution is due to the application of LTEA+CD and not due to any manual enhancement of resolution there.

When stations are gathered into more regional groups, there is almost no distinction among the three meshes (Table IV).

11. DISCUSSION

We have demonstrated the applicability of LTEA+CD to a large-scale domain having detailed features on the order of 1–10 km. LTEA+CD allows the computation of target element sizes over the entire domain, including the boundary. These target element sizes were applied in the mesh module of SMS to produce automatically the corresponding meshes.

LTEA+CD has the potential to provide target element sizes for a mesh having fewer nodes than an initial mesh, while performing similarly in terms of the solution. Results indicate that the INTR mesh is an improvement over ec2000v2d because it contains 14% fewer nodes and elements and is, overall, equally skilled in producing elevation tides.

This paper has shown how LTEA+CD may be applied effectively to produce meshes that are as accurate or are more accurate than those produced with other, subjective methods. Because LTEA+CD is applicable throughout the model domain, the method enables the nearly automatic production of efficient and accurate meshes over realistic domains, as demonstrated over the large-scale WNAT model domain. Only a minor flaw (resulting in the generation of correctible errors in the mesh adjacent to the boundary) in SMS prevented the fully automatic meshing of the WNAT domain.

We would expect that inclusion of additional coastline detail will influence the results produced by LTEA+CD and therefore the corresponding mesh. For example, Blanton *et al*. [34] showed that the inclusion of the estuary/tidal inlet complex in the South Atlantic Bight promoted a more realistic description of shelf flow in an ADCIRC model. Since our domain has no particular area of interest, we have not included such details.

Perhaps the limitation imposed upon the minimum element size in the FIN mesh precludes it from performing better than either of the other two meshes, which have elements smaller than 1000 m in certain locations. Lifting the imposition of the 1000 m minimum element size is impractical with regard to our emphasis here on an application. Doing so results in meshes having over one million elements—too many, in our judgment, to be practical for our computing facilities.

Our experiments, including those presented in this paper, have not produced a convergent series of meshes although an iterative mesh generation method has been applied. In preliminary trials, meshes in a series produced iteratively show that in regions of relatively complicated flow, proportionately more and more nodes are demanded by LTEA+CD, and vice versa. This is not a desirable property of LTEA+CD; however, it is consistent with the fact that representation of relatively complicated flow fields requires relatively high resolution. While we have not found

DOI: 10.1002/fld

a means of causing the meshes to converge, we have, in another paper [1] and for a simplified case, demonstrated *solution* convergence under iterative application of LTEA−CD (note the minus sign).

LTEA+CD surpasses the capabilities of existing mesh generation techniques by combining the idealism of localized truncation error analysis with the power of complex derivatives resulting in a new, efficient target element size calculator that is applicable not only on the interior of the domain, but also at the boundary (LTEA fails within about four elements of the boundary), so that target element sizes may be computed for bodies of water containing complicated boundaries.

LTEA+CD accounts for Coriolis force and variable bottom stress in the target element size calculator itself. Both Coriolis force and bottom stress are important factors under LTEA+CD. Both provide significant influence of the target element sizes; Coriolis force is significant throughout the WNAT model domain, while bottom stress is significant only in shallow waters, such as the continental shelf.

Near the domain boundary, nonlinearities become more important. LTEA+CD accounts for all nonlinearities indirectly, namely by analyzing all tidal constituents (including over tides and shallow water tides), which, in turn, have the opportunity to interact with one another in a fully nonlinear simulation.

LTEA+CD provides the means to determine automatically target element sizes and, with the aid of a mesh generator such as SMS, to generate automatically an actual mesh.

In the present study, ADCIRC and its discrete form of the momentum equations has been applied in developing LTEA+CD. Therefore Equation (7) should be applied only to modeling problems having similar mathematics. However, it is expected that the principles of LTEA+CD may be applied to other models.

Target element sizes computed with LTEA+CD are scaleable through an arbitrary parameter a. Herein, a single, domain-wide value of a is applied to the generation of each mesh. However, one may also vary the parameter throughout the domain, providing enhanced resolution in an area of interest, for example. Herein, an automatic process for the determination of a has also been developed and used with success.

12. CONCLUSIONS

We recommend that tidal modelers consider applying LTEA+CD to the automatic construction of FE meshes for tidal model domains. Furthermore, indications are that LTEA-based meshes are appropriate for storm surge applications—cf. [35, 36]; therefore it is also recommended that storm surge modelers consider LTEA+CD when developing meshes for their model domains.

These LTEA+CD-based meshes are reflective of the flow field and of the bathymetric features of the domain, and produce accurate results. They account for physical processes, namely bottom stress and Coriolis force, unlike meshes produced with other mesh generation criteria.

Herein, LTEA+CD has been demonstrated to produce meshes having reduced numbers of elements compared to initial high-resolution meshes. The reduction of the number of elements with the maintenance of accuracy should benefit studies in which multiple simulations must be performed as well as applications in operational environments where quick turn-around time is critical.

Although LTEA+CD has been herein applied *a posteriori*, it may be applied *a priori* if sufficient measurement-based data (WSE and velocity fields) are available; measurements may be taken from the field or from physical models. We envision a future in which depth-integrated velocities

DOI: 10.1002/fld

over the globe could be measured via remote sensing technology. A resultant data set could be used in an application of LTEA+CD. It is already possible to measure not only depth-integrated velocities, but velocity profiles also by using acoustic Doppler current profilers; Visbeck [37] provides an example application. Mollo-Christensen *et al*. [38] estimate ocean current velocity using an infrared image. Crocker *et al*. [39] discuss some of the difficulties related to estimating surface currents from infrared and ocean color satellite imagery.

Since we are now able to include locally variable bottom friction and are able to compute the target element sizes at and near the boundary, it makes sense to extend the application of LTEA+CD into coastal water bodies such as an estuary. Just such applications are part of our continuing research. The inclusion of coastal features such as smaller embayments (e.g. the estuary/tidal inlet complex of the South Atlantic Bight) flows logically from the demand of LTEA+CD for more resolution in those areas.

ACKNOWLEDGEMENTS

This research was in part conducted under award NA04NWS4620013 from the National Oceanic and Atmospheric Administration (NOAA), US Department of Commerce. The statements, findings, conclusions, and recommendations are those of the authors and do not necessarily reflect the views of NOAA or the Department of Commerce.

This research was in part conducted under Award N00014-02-1-0150 from the National Oceanographic Partnership Program (NOPP) administered by the Office of Naval Research (ONR). The statements, findings, conclusions, and recommendations are those of the authors and do not necessarily reflect the views of ONR or NOPP and its affiliates.

The authors gratefully acknowledge the support of the College of Engineering & Computer Science and the I2Lab at the University of Central Florida.

REFERENCES

1. Parrish DM, Hagen SC. 2D, unstructured mesh generation for oceanic and coastal tidal models from a localized truncation error analysis with complex derivatives. *International Journal of Computational Fluid Dynamics* 2007; **21**(7–8):277–296. DOI: 10.1080/10618560701582500.
2. Hagen SC. Finite element grids based on a localized truncation error analysis. *Ph.D. Thesis*, University of Notre Dame, South Bend, IN, 1998.
3. Hagen SC. Estimation of the truncation error for the linearized, shallow water momentum equations. *Engineering with Computers* 2001; **17**(4):354–362.
4. Hagen SC, Westerink JJ, Kolar RL. One-dimensional finite element grids based on a localized truncation error analysis. *International Journal for Numerical Methods in Fluids* 2000; **32**(2):241–261. DOI: 10.1002/(SICI)1097-0363(20000130)32:2<241::AID-FLD947>3.0.CO;2-#.
5. Hagen SC, Westerink JJ, Kolar RL, Horstman O. Two-dimensional, unstructured mesh generation for tidal models. *International Journal for Numerical Methods in Fluids* 2001; **35**(6):669–686.
6. Westerink JJ, Luettich Jr RA, Muccino JC. Modeling tides in the western North Atlantic using unstructured graded grids. *Tellus* 1994; **46A**:178–199.
7. Luettich Jr RA, Westerink JJ. Continental shelf scale convergence studies with a Barotropic Tidal model. In *Quantitative Skill Assessment for Coastal Ocean Models*, Coastal and Estuarine Studies 47, Lynch DR, Davies AM (eds). American Geophysical Union: Washington, DC, 1995; 349–371.
8. Loder JW. Topographic rectification of tidal currents on the sides of Georges Bank. *Journal of Physical Oceanography* 1980; **10**(9):1399–1416.
9. Lynch D, Ip J, Naimie C, Werner F. Convergence studies of tidally rectified circulation on Georges Bank. In *Quantitative Skill Assessment for Coastal Ocean Models*, Coastal and Estuarine Studies 47, Lynch DR, Davies AM (eds). American Geophysical Union: Washington, DC, 1995; 153–174.

10. Hannah CG, Wright DG. Depth dependent analytical and numerical solutions for wind-driven flow in the coastal ocean. In *Quantitative Skill Assessment for Coastal Ocean Models*, Coastal and Estuarine Studies 47, Lynch DR, Davies AM (eds). American Geophysical Union: Washington, DC, 1995; 125–152.
11. Greenberg DA, Dupont F, Layard FH, Lynch DR, Werner FE. Resolution issues in numerical models of oceanic and coastal circulation. *Continental Shelf Research* **27**(9):1317–1343. DOI: 10.1016/j.csr.2007.01.023.
12. Foreman MGG. A two-dimensional dispersion analysis of selected methods for solving the linearized shallow water equations. *Journal of Computational Physics* 1984; **56**(2):287–323.
13. Le Provost C, Genco ML, Lyard F. Modeling and predicting tides over the world ocean. In *Quantitative Skill Assessment for Coastal Ocean Models*, Coastal and Estuarine Studies 47, Lynch DR, Davies AM (eds). American Geophysical Union: Washington, DC, 1995; 175–201.
14. Le Provost C, Vincent P. Some tests of precision for a finite element model of ocean tides. *Journal of Computational Physics* 1986; **65**(2):273–291.
15. Kashiyama K, Okada T. Automatic mesh generation method for shallow water flow analysis. *International Journal for Numerical Methods in Fluids* 1992; **15**(9):1037–1057.
16. Westerink JJ, Luettich Jr RA, Baptista AM, Scheffner NW, Farrar P. Tide and storm surge predictions using finite element model. *Journal of Hydraulic Engineering* 1992; **118**:1373–1390.
17. Hagen SC, Horstman O, Bennett RJ. An unstructured mesh generation algorithm for shallow water modeling. *International Journal of Computational Fluid Dynamics* 2002; **16**(2):83–91.
18. Hagen SC, Parrish DM. Meshing requirements for tidal modeling in the Western North Atlantic. *International Journal of Computational Fluid Dynamics* 2004; **18**(7):585–595. DOI: 10.1080/10618560310001596819.
19. Greenberg MD. *Advanced Engineering Mathematics* (2nd edn). Prentice-Hall: Upper Saddle River, NJ, 1998; 1177–1178.
20. Daugherty RL, Franzini JB, Finnemore EJ. *Fluid Mechanics with Engineering Applications* (8th edn). McGraw-Hill: New York, 1985; 142–143.
21. Reddick HW, Miller FH. *Advanced Mathematics for Engineers* (3rd edn). Wiley: New York, 1938; 426–433.
22. Saada AS. *Elasticity*: *Theory and Applications*. Pergamon: New York, 1974; 210.
23. Timoshenko SP, Goodier JN. *Theory of Elasticity* (3rd edn). McGraw-Hill: New York, 1970; 18, 58.
24. Sadd MH. *Elasticity*: *Theory*, *Applications*, *and Numerics*. Elsevier: Burlington, MA, 2005; 249.
25. Weisstein EW. Cauchy–Riemann Equations. Available online at: http://mathworld.wolfram.com/Cauchy-RiemannEquations.html (accessed 9 June 2006).
26. Hagen SC, Zundel AK, Kojima S. Automatic, unstructured mesh generation for tidal calculations in a large domain. *International Journal of Computational Fluid Dynamics* 2006; **20**(8):593–608.
27. Luettich Jr RA, Westerink JJ. Formulation and Numerical Implementation of the 2D/3D ADCIRC Finite Element Model Version 44.XX. 2004. Available online at: http://www.adcirc.org/adcirc_theory_2004_12_08.pdf (accessed 10 February 2007).
28. Luettich Jr RA, Westerink JJ, Scheffner NW. ADCIRC: an advanced three-dimensional circulation model for shelves, coasts and estuaries, report 1: theory and methodology of ADCIRC-2DDI and ADCIRC-3DL. *Dredging Research Program Technical Report DRP-92-6*, US Army Corps of Engineers, Washington, DC, 1992.
29. Mukai AY, Westerink JJ, Luettich Jr, Mark D. Eastcoast 2001, a tidal constituent database for the Western North Atlantic, Gulf of Mexico and Caribbean Sea. US Army Corps of Engineers, Washington, DC, 2001.
30. BYU. *Surface–water modeling system* v 9.0. Brigham Young University: Provo Ut, 2005 (Software; Build Date 9 June 2006).
31. NGDC (National Geophysical Data Center). World Data Bank II coastline database. Available online at: http://rimmer.ngdc.noaa.gov/coast/ (accessed 1 November 2006).
32. Kojima S. Optimization of an unstructured finite element mesh for tide and storm surge modeling applications in the Western North Atlantic Ocean. *Master's Thesis*, University of Central Florida, Orlando, 2005.
33. Werner FE. A field test case for tidally forced flows: a review of the tidal flow forum. In *Quantitative Skill Assessment for Coastal Ocean Models*, Coastal and Estuarine Studies 47, Lynch DR, Davies AM (eds). American Geophysical Union: Washington, DC, 1995; 269–283.
34. Blanton BO, Werner FE, Seim HE, Luettich Jr RA, Lynch DR, Smith KW, Voulgaris G, Bingham FM, Way F. Barotropic tides in the South Atlantic Bight. *Journal of Geophysical Research* 2004; **109**:C12024. DOI: 10.1029/2004JC002455.
35. Bennett RJ. Finite element grid development for the Waccamaw River: a reproducible Approach. *Master's Thesis*, University of Central Florida, Orlando, 1999.

36. Hagen SC, Dietsche D, Funakoshi Y. Storm tide hindcasts for hurricane Hugo: into an estuarine and riverine system. *Proceedings*, *Sixth International Conference on Hydro-Science and Engineering*, Brisbane, Australia, 30 May–4 June 2004.
37. Visbeck M. Deep velocity profiling using lowered acoustic Doppler current profilers: bottom track and inverse solutions. *Journal of Atmospheric and Oceanic Technology* 2002; **19**(5):794–809.
38. Mollo-Christensen E, Cornillon P, Da S, Mascarenhas A. Method for estimation of ocean current velocity from satellite images. *Science New Series* 1981; **212**(4495):661–662.
39. Crocker RI, Matthews DK, Emery WJ, Baldwin DG. Computing coastal ocean surface currents from infrared and ocean color satellite imagery. *IEEE Transactions on Geoscience and Remote Sensing* 2007; **45**(2):435–447.

DOI: 10.1002/fld